VTT Technical Research Centre of Finland

High-Throughput Tailoring of Nanocellulose Films

Khakalo, Alexey; Mäkelä, Tapio; Johansson, Leena-Sisko; Orelma, Hannes; Tammelin, Tekla

Published in:
ACS Applied Bio Materials

DOI:
10.1021/acsabm.0c00576

Published: 01/01/2020

Document Version
Publisher's final version

ACS APPLIED BIO MATERIALS

www.acsabm.org Article

High-Throughput Tailoring of Nanocellulose Films: From Complex Bio-Based Materials to Defined Multifunctional Architectures

Alexey Khakalo,* Tapio Mäkelä, Leena-Sisko Johansson, Hannes Orelma, and Tekla Tammelin*

Cite This: *ACS Appl. Bio Mater.* 2020, 3, 7428−7438 Read Online

ACCESS | Metrics & More | Article Recommendations | Supporting Information

ABSTRACT: This paper demonstrates a high-throughput approach to fabricate nanocellulose films with multifunctional performance using conventionally existing unit operations. The approach comprises cast-coating and direct interfacial atmospheric plasma-assisted gas-phase modification along with the microscale patterning technique (nanoimprint lithography, NIL), all applied in roll-to-roll mode, to introduce organic functionalities in conjunction with structural manipulation. Our strategy results in multifunctional cellulose nanofibrils (CNF) films in which the high optical transmittance (∼90%) is retained while the haze can be adjusted (2−35%). Concomitantly, the hydrophobic/hydrophilic balance can be tuned (50−21 mJ/m^2 with the water contact angle ranging from ∼20 up to ∼120°), while intrinsic hygroscopicity of CNF films is not significantly compromised. Therefore, a challenge to produce multifunctional bio-based materials with properties defined by various high-performance applications conjoined to the lack of efficient processing strategies is elucidated. Overall, economically and ecologically viable strategy, which was realized by facile and upscalable unit operations using the R2R technology, is introduced to expand the properties' spaces and thus offer a vast variety of interesting applications for CNF films.

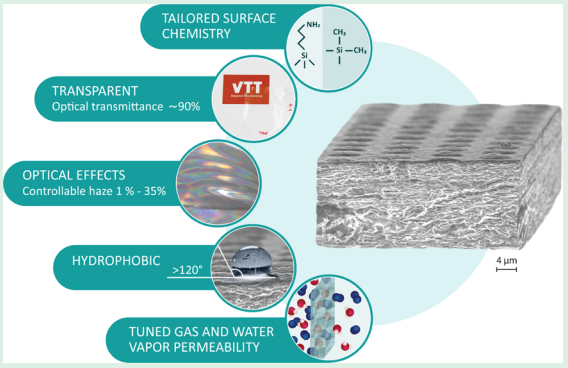

KEYWORDS: *cellulose nanofibrils film, light management, surface chemical modification, plasma polymerization, hydrophobic and barrier coating*

INTRODUCTION

Films fabricated from plant-derived nanoscaled cellulosic materials (cellulose nanofibrils, CNF) are increasingly considered to be exploited in, e.g., green (printed) electronics, biological devices, and energy applications due to their inherent and unique physical properties.[1,2] Two-dimensional nanocellulose architectures appear as translucent or even fully transparent films; they possess high thermal stability, moderate smoothness, piezoelectric and dielectric properties, birefringency, optical properties, and low density coupled with relatively high strength, among many others, and their structural and chemical modification is moderately easy.[3−8] In this context, as defined by many high-performance applications, intriguing inherent properties of CNF structures coupled with several options to exploit materials tunability offer prospects for the development of multifunctional materials derived from renewable sources. However, a grand challenge often lies in the lack of facile and upscalable manufacturing and processing methods to fabricate such materials with bio-based status in which the inherent features are efficiently exploited. This drastically limits the industrial adoption of multifunctional systems within emerging fields of "green" optoelectronics, electronics, energy, and sensing applications, especially when high throughput is needed.

2,2,6,6-Tetramethylpiperidine-1-oxyl (TEMPO)-CNF, which is produced by 2,2,6,6-tetramethylpiperidine-1-oxyl (TEMPO) radical-mediated oxidation of cellulosic fibers, is considered as a very attractive nanocellulose grade since self-standing TEMPO-CNF films are fully transparent with a low surface roughness.[9] As previously reported, TEMPO-oxidized nanofibers can be integrated in such systems where high haze and high transparency are essential. Fang et al. achieved such a combination by drying under pressure wet film of TEMPO-oxidized nanofibers placed between two stacks of regular filter paper.[10] Alternatively, nanostructured papers with both high transparency (>91%) and high haze (>89%) were obtained by partly dissolving and in situ nanowelding in ionic liquid (IL) microfibers[11] or fabricated directly from original paper with rapid IL-polishing processes.[12] Simple deposition (coating) of microsized TEMPO-oxidized wood fibers was utilized to tune the optical haze of the films made from TEMPO-oxidized

Received: May 17, 2020
Accepted: October 15, 2020
Published: October 29, 2020

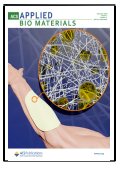

https://dx.doi.org/10.1021/acsabm.0c00576
ACS Appl. Bio Mater. 2020, 3, 7428−7438

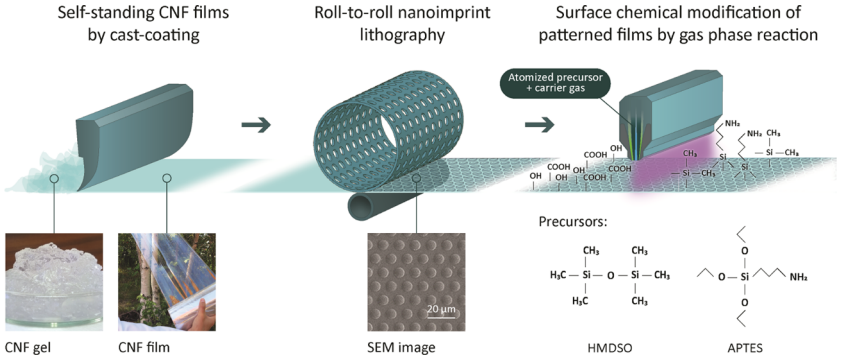

Figure 1. Schematic illustration of roll-to-roll manufacturing and modification strategy of multifunctional TEMPO-CNF films combining nanoimprint lithography (NIL) to create micropillar patterns and plasma-enhanced chemical vapor deposition for simple interfacial modification using APTES and HMDSO as precursors. Photographs showing initial appearance of nanocellulose gel that forms a transparent continuous film upon drying. SEM image illustrates features of NIL surface-patterned TEMPO-CNF film.

cellulose nanofibrils by increasing the light scattering on the upper surface.[13] High material transparency accompanied with high haze is particularly beneficial for outdoor displays and solar cells.

Cellulose nanofibrils are extremely hygroscopic—an untapped property, which has often been considered as a disadvantage interfering the full utilization of bio-based building blocks. The potential deriving from this feature is, however, convincingly evidenced. For example, a combination of hygroscopicity with advanced light management is an attractive feature for photosynthetic cell factories.[7] Water vapor-induced swelling and film softening facilitate mechanical nanoimprint lithography (NIL) process when the nanocellulose film is periodically patterned to generate optical effects.[14] In addition, microfluidic cellulose-based analytical devices appear as a promising platform for disposable, high-efficiency, and portable systems for use in environmental monitoring, health diagnostics, and food quality testing.[15] The devices make use of the capillary force (with no assistance of external forces) to transport fluid along well-defined hydrophobic patterns.[18] Highly hydrophobic cellulosic materials while retaining their breathability and moisture buffering ability were achieved via layer-by-layer deposition of two natural components, cationic poly-L-lysine, and anionic carnauba wax particles for their use as functional textiles.[16] A biodegradable, fully organic (cellulose/wax-based), and hierarchically textured superhydrophobic material was reported.[17] The material consisted of a cellulose micropatterned substrate coated with a carnauba wax layer, which lowered the surface energy of the substrate and induced a second order of roughness at the same time.

Atmospheric pressure plasma-enhanced chemical vapor deposition technology allows a uniform one-step tailoring of substrate's surface chemistry in large-scale production.[18,19] During plasma polymerization of organosilicon compounds, monomer is dissociated by breaking the bonds through collision with electrons, and then the formed radicals/fragments are deposited directly on the substrate surface forming a growing film.[20] One of the most commonly used siloxane, hexamethyldisiloxane (HMDSO), a monomer that otherwise cannot be polymerized following the conventional methodologies in liquid phase, undergoes polymerization under plasma conditions by rearranging the radicals produced during its dissociation.[21] By this way, stable hydrophobic layers can be formed on, e.g., polyimide films,[22] filter papers, and cotton clothes,[23] due to the high retention of methyl groups. Another interesting group, amine-containing precursors, e.g., 3-aminopropyl-triethoxysilane (APTES), allow surface functionalization with free reactive nitrogen-containing groups, particularly primary amines ($-NH_2$), which are widely utilized in bio-devices such as advanced drug-delivery systems, cell microarrays, and biosensors to assist cell or enzyme attachment through the formation of covalent bonds with carboxyl group present in biomolecules.[24,25] Previously, we have demonstrated how this particular aminosilane group efficiently prevents the permeability of oxygen molecules into the nanocellulose films in the presence of water molecules.[26]

In this work, we report a simple and upscalable surface modification strategy to produce and tailor nanocellulose films using on-line techniques, which are compatible with industrial lines. The purpose is to fabricate films with peculiar optical performance, tunable hydrophobic/hydrophilic balance, and controlled gas and vapor transport properties without compromising the intriguing physical properties provided by cellulose nanofibrils, such as transparency and hygroscopicity. To show multifunctionality, we demonstrate a synergistic fabrication procedure, which combines mechanical NIL patterning of cast-coated nanocellulose films with plasma-assisted single-layer deposition of well-defined chemical groups of either HMDSO or APTES, as schematically illustrated in Figure 1. NIL patterns manipulate optical response via formation of continuous arrays. Besides, micropatterning is a route to adjust the roughness profile of the nanocellulose film. HMDSO groups introduced on the already assembled nanocellulose film surfaces tailor the surface energy and wettability of the films, whereas APTES groups reduce moisture sensitivity due to self-condensation reactions taking place. The chemical composition of the CNF film structures was carefully characterized using X-ray photoelectron spectroscopy (XPS) and energy-dispersive X-ray spectroscopy (EDS), whereas the morphological details were investigated by atomic force microscopy (AFM) and scanning electron microscopy (SEM). Furthermore, several physical properties were revealed to evidence the multifunctional character, i.e., surface energy, transparency accompanied with haze, as well as oxygen and moisture permeabilities.

RESULTS AND DISCUSSION

Optical Properties, Surface Free Energy, Wettability, and Oxygen/Water Vapor Permeability of Surface-

https://dx.doi.org/10.1021/acsabm.0c00576
ACS Appl. Bio Mater. 2020, 3, 7428−7438

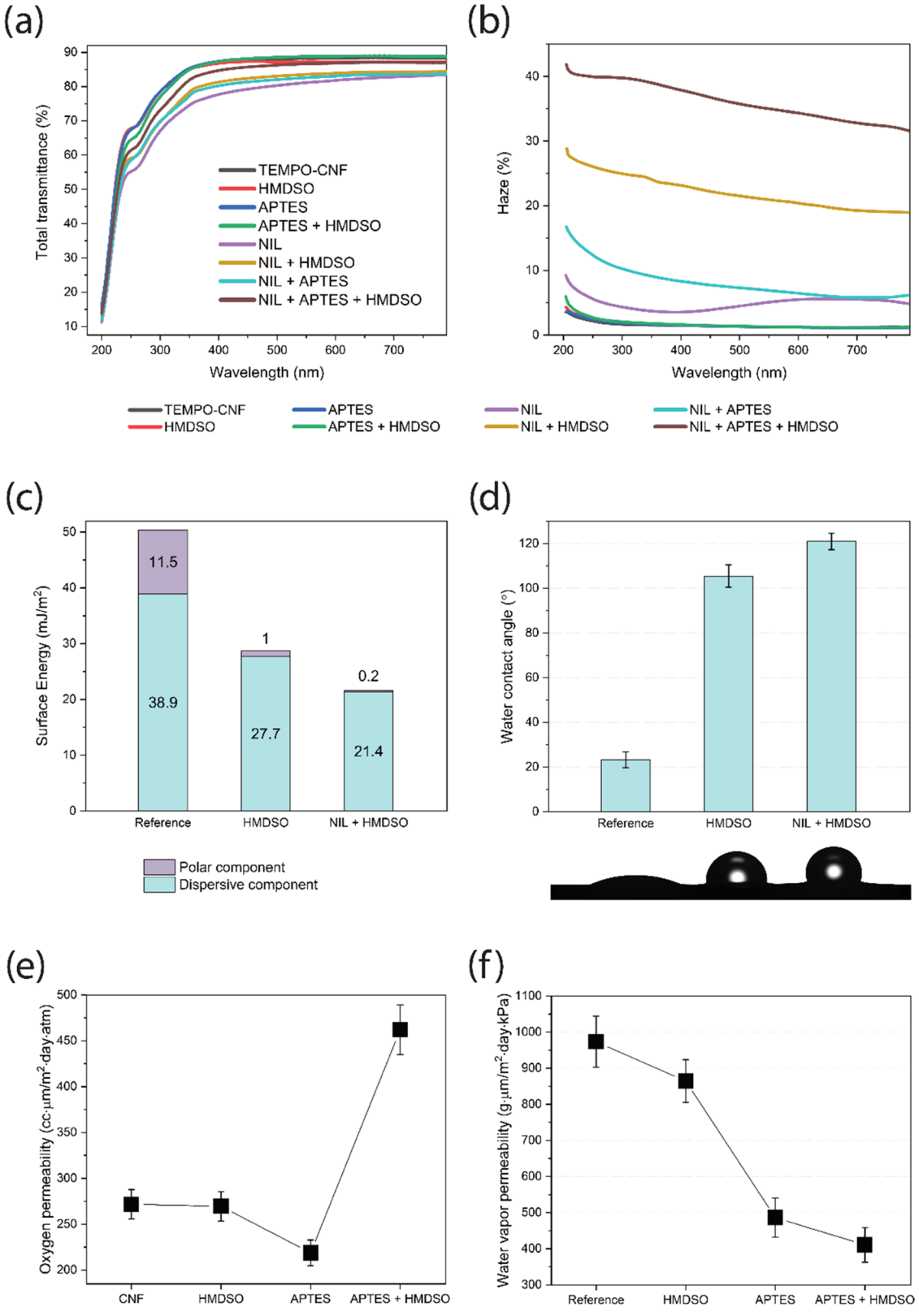

Figure 2. Surface NIL patterning combined with plasma deposition allows simple and upscalable tailoring of TEMPO-CNF films properties: transparency of the surface-modified TEMPO-CNF films (a) is maintained while simultaneously giving possibility to introduce optical haze (b); moreover, surface free energy (c), hydrophobicity (d) as well as oxygen (e) and water vapor (f) permeability can be manipulated.

Tailored TEMPO-CNF Films. Light transmittance of the NIL surface-patterned and plasma-deposited TEMPO-CNF films was investigated in the visible-light wavelength range, as demonstrated in Figure 2a. TEMPO-CNF films fabricated from nanosized fibers have extremely low scattering in the visible light as the diameter of such fibers (<10 nm) is much smaller than the wavelength of the visible light (390−760 nm). Moreover, assembled films have low porosity and compact

https://dx.doi.org/10.1021/acsabm.0c00576
ACS Appl. Bio Mater. 2020, 3, 7428−7438

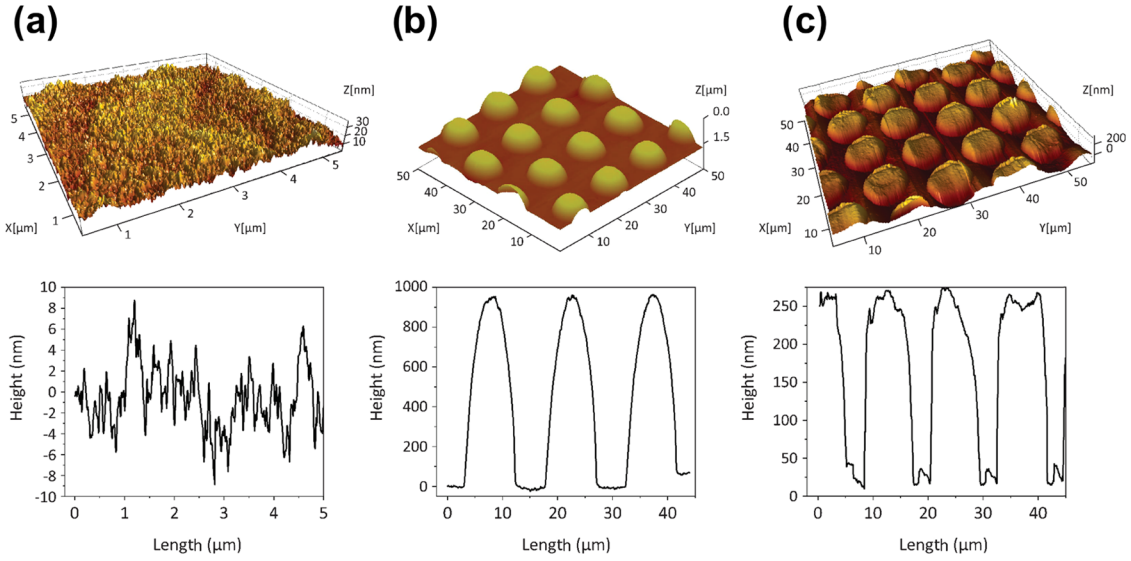

Figure 3. AFM three-dimensional (3D) topography images (top) with height scan profiles (bottom) of reference TEMPO-CNF film (a), NIL surface-patterned TEMPO-CNF film (b) and TEMPO-CNF film after NIL surface patterning and HMDSO plasma deposition (c).

structure, which weaken the light scattering between fibers and air, resulting in high transparency (about 90% at 600 nm) of the TEMPO-CNF films.[27] The TEMPO-CNF film was transparent with ~90% total light transmittance at a wavelength of 550 nm; see also Figure 1. All plasma-deposited TEMPO-CNF films showed nearly the same level of light transmittance (88−89% at 550 nm) as that of a pure substrate. According to Snell's law, light is diffracted as it passes through an interface,[28] for example, the higher the difference in refractive indexes of the two media, the higher the diffraction angle will be. The refractive index of cellulose is 1.53,[29] whereas it is a bit lower for PP-HMDSO (refractive index = 1.47)[30] and APTES (refractive index ≈ 1.42).[31] However, the presented results indicated almost no influence on the transparency of the TEMPO-CNF films upon plasma depositions since all electromagnetic waves within visible-light wavelength maintained its original direction when transmitted through the samples. Moreover, void-free, uniform, and dense layers were produced, which would otherwise affect the samples' transmittance due to refractive index mismatch between cellulose, depositions, and air (refractive index = 1.0). Upon combined NIL patterning and plasma deposition, the optical transmittance remained in the range 82−90%, indicating almost fully transparent films at a wavelength of 550 nm. NIL-patterned and plasma-treated samples showed higher order of diffraction and thereby substantial light scattering, which led to a higher optical haze (quantifies the percentage of the forward light scattering), as shown in Figure 2b. The values as high as 35% at 550 nm were reached, whereas haze <2% was observed both for reference and plasma-deposited TEMPO-CNF films. The rough surface of NIL-patterned and plasma-deposited samples (Figure 3) caused prominent light scattering of surfaces with various roughnesses. This finding is in accordance with the previous studies of multilayers structure involving TEMPO-CNF and wood fibers.[32] To summarize, plasma-deposited TEMPO-CNF films showed excellent light transmittance (88−89% at 550 nm) and low optical haze (<2% at 550 nm), making them attractive for indoor high-definition display devices that require high clarity. On the other hand, the scattering of films subjected to surface patterning and plasma deposition (optical haze, 35% and transmittance, ca. 83−87% at 550 nm) can lead to an antiglare effect, which is widely used in outdoor displays where devices operate in a bright environment. In addition, high haze accompanied with high clarity is beneficial in solar cell applications as light will be trapped in the solar cell for a longer time, thus leading to better solar cell efficiency.[10,33]

To evaluate the changes in surface energy (SE) of NIL surface-patterned and plasma-deposited TEMPO-CNF films, the average CAs for liquids with various surface tensions were determined and the dispersive as well as acid and base contributions of the surface energy were derived according to the acid−base theory (Figures 2c and S1a, Table S1). SE of the TEMPO-CNF film (γs ~ 51 mJ/m^2) is within the range of previously reported values for cellulosic nanofibrils, 44−54 mJ/m^2.[34] The effect of HMDSO deposition on the SE of TEMPO-CNF films is substantial, whereas that of APTES is less pronounced. Upon HMDSO deposition, the surface energy decreases through both the dispersive and polar components, which is rational given the introduction of new functionalities onto cellulose surface (nonpolar Si-$(CH_3)_3$ groups replaced hydroxyl groups in cellulose; see below). Contrarily, the SE of APTES layer deposited on TEMPO-CNF film even becomes higher compared to base substrate due to terminal amine functionalities of APTES (see below). Combined with surface NIL patterning, the SE of the respective depositions was found to decrease in all cases (Figures 2c and S1a). For example, SE as low as 21.6 mJ/m^2 was reached for NIL surface-patterned and HMDSO-deposited films, which is composed only of the dispersive component (γ^d). Meanwhile, the polar component drops from 11.5 down to 0.2 mJ/m^2. Table S1 reveals also a strong electron-donating tendency for the cellulosic surfaces (the electron donor, Lewis base, component clearly dominates over that of the electron acceptor, Lewis acid component ($\gamma^- \gg \gamma^+$)), thus indicating the ability to participate in polar interactions with other acidic moieties. HMDSO layer deposition onto the TEMPO-CNF surface significantly reduced γ^- from 53.3 to 0.3 mJ/m^2. Simultaneously, the acid component contribution increased and, as a result, the ratio of the base and acid components (γ^-/γ^+) is strongly reduced. It is

https://dx.doi.org/10.1021/acsabm.0c00576
ACS Appl. Bio Mater. 2020, 3, 7428−7438

worth mentioning that an increased γ^+ parameter not only indicates amphoteric properties of the surface but also would allow interactions of modified TEMPO-CNF with other bipolar species. Amphoteric nature (acid and base) becomes even more pronounced upon APTES deposition.

The affinity to water of the modified films was derived based on the interfacial free energy of interaction, ΔG_{sws}^{IFE}, between water and chemical groups introduced to the solid substrate (Table S1). When ΔG_{sws}^{IFE} is positive, the water−substrate interactions dominate over the cohesive attraction within the polar water molecules and, therefore, the surface of the substrate is expected to be hydrophilic. In contrast, negative ΔG_{sws}^{IFE} suggests the substrate immersed in water to be hydrophobic as it avoids contact with water molecules due to high cohesive energy.

This implies that the sign of ΔG_{sws}^{IFE} determines the character of the material surface and the value of ΔG_{sws}^{IFE} may be considered as a quantitative indication of the extent of surface hydrophobicity. Positive ΔG_{sws}^{IFE} for TEMPO-CNF films highlights the dominant hydrophilic nature of cellulosic surface. Plasma deposition of HMDSO and APTES layers varies the surface character of cellulose, turning it to hydrophobic (positiveΔG_{sws}^{IFE}), whereas the hydrophobicity of the HMDSO layer is higher than the one of APTES layer (4- to 6-fold difference in ΔG_{sws}^{IFE}, on average).

The effects of different depositions as well as surface patterning on the water contact angle (WCA) are presented in Figures 2d and S1b. It is well documented that surface energy and surface roughness are the main factors influencing the material wettability.[35] Low surface energy accompanied with hierarchical surface roughness of the material results in a surface with improved hydrophobicity.[36] Neat TEMPO-CNF films showed WCA values ∼25°, which are typical for the hydrophilic cellulose surfaces.[37] The wetting behavior of TEMPO-CNF substrate was significantly changed after plasma deposition: equilibrium WCA reached values of ∼105° and ∼70° for HMDSO (Figure 2d) and APTES (Figure S1b) layers, respectively. These observations are in good accordance with the values reported for the given modification strategies. For example, WCA of 95° has been documented for the nanofibrillated cellulose film surface after HMDSO gas-phase modification.[38] Hydrophobic deposition onto natural leather realized via a plasma polymerization of HMDSO resulted in WCA values of ∼110° depending on the deposition parameters.[39] Moreover, values as high as 115° were attained for polyethylene[21] and polyimide[22] substrates with thin layers deposited from pure HMDSO vapors in plasma reactors. For APTES-modified surfaces, WCA values of 65−73° were reported for thermoplastic substrates. An increase in WCA from 16° up to 75° and from 22° up to 65° was observed for APTES-modified prehydrophilized gold[40] and activated glass,[41] respectively. Figure 2d indicates that the WCA of NIL-patterned and HMDSO plasma-coated TEMPO-CNF films reached a value of 121°.

Hydrophilic and densely packed TEMPO-CNF films effectively retard the oxygen permeability at relatively dry conditions (<50% RH).[42] However, in moist conditions (when exposed to an environment with RH >65%), the hydrogen-bonding network responsible for interactions between individual fibrils within the CNF film gets disturbed. Therefore, surface modifications of the assembled CNF structures are required to prevent the oxygen permeability at high humidity conditions. Figure 2e illustrates the influence of plasma deposition on the oxygen permeability of TEMPO-CNF films. It should be noted that selected testing conditions (23 °C and 80% RH) are rather harsh for cellulosic materials. HMDSO deposition seems to have a minor effect on the oxygen permeability (OP) through the films' structure, which could be attributed to the enhanced affinity of oxygen (a molecule of low polarity) toward introduced nonpolar Si−$(CH_3)_3$ groups compared to the highly polar functionalities (carboxyl and hydroxyl groups) present in unmodified TEMPO-CNF (see previous section). Change in surface energy due to APTES deposition results in a reduced oxygen permeability at 80% RH, yielding OP values of ∼220 $cm^3 \cdot \mu m/(m^2 \cdot day \cdot atm)$. The achieved permeability values are significantly lower compared to the synthetic polymers, such as PET, LDPE, and PP, which have permeability values of 1500, 2200, and 93000 $cm^3 \cdot \mu m/(m^2 \cdot day \cdot atm)$ in the same conditions of 80% RH, respectively. Also, APTES deposited samples measured at 38 °C and 95% RH showed OP values of 12960 ± 540 $cm^3 \cdot \mu m/(m^2 \cdot day \cdot atm)$.

In general, depositions retard permeation through the substrate by blocking the oxygen flow passing through it (unless any available defects in the coating). This is in contrast to the behavior of water molecules that are prone to interact and react with deposited layers. Therefore, water vapor permeation (WVP) through the deposition is significantly influenced by the chemical interactions of water vapor with the deposition as well as its microstructure. Plasma depositions tend to lower the water vapor permeability of TEMPO-CNF films, as depicted in Figure 2f, due to the formation of cross-linked structures with −Si−O−Si− bonds. Moreover, chemical effects might also play a role here. Water has lone-pair electrons and a large dipole moment, and thus is a good electron donor. Therefore, strong molecular adsorption can occur by acid/base interactions between water vapor and the deposition surface (see Table S1) with the generation of OH groups. The thus-formed OH groups can be located on the top surface as well as the internal surface of pores, both of which are a pathway of water vapor flow through the deposition and may prevent the continuous penetration of water vapor through the substrate.[43]

Thickness and Morphology of Plasma-Deposited Layers. The thickness and surface morphology of the plasma depositions onto TEMPO-CNF films (layer order: HMDSO-APTES-TEMPO-CNF) were investigated by means of SEM and AFM. The EDX data of the coatings further confirmed the successful deposition of APTES and HMDSO layers via the presence of Si signal, which is considered as a marker for both of the layers, whereas the underlying TEMPO-CNF substrate was free from Si (Figure 4). The deposited layers were rather uniform, and the thicknesses of APTES and HMDSO layers were ∼390 and ∼850 nm, respectively. Previously, we have shown that the heights of pillars on patterned CNF films are ∼1.5 μm,[44] and the thickness of, for example, hybrid APTES-HMDSO layers, is ∼1.3 μm. Thus, the printed pillars on TEMPO-CNF substrates are well preserved, as was shown in Figure 3c, but the structural height of the patterned films was lowered due to plasma deposition. For this reason, light transmittance of the NIL-patterned TEMPO-CNF films increased with thicker deposited layer (see previous section), while gain in WCA of NIL-patterned and HMDSO-coated films, ∼15°, is smaller than for NIL-patterned and APTES-coated films, ∼20° (Figure S1b).

https://dx.doi.org/10.1021/acsabm.0c00576
ACS Appl. Bio Mater. 2020, 3, 7428−7438

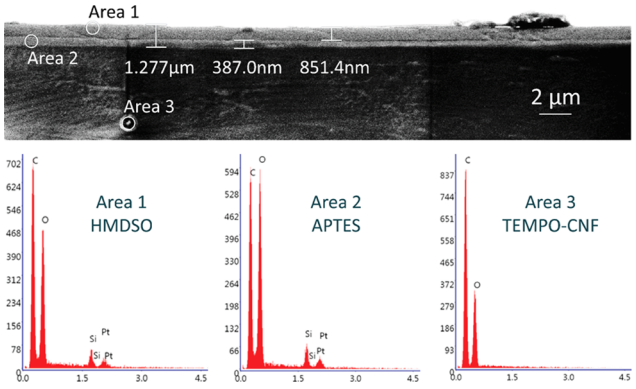

Figure 4. Cross-sectional SEM image (top) and EDX data (bottom) of the plasma-assisted depositions on TEMPO-CNF film showing the thicknesses of APTES and HMDSO submicron layers.

The AFM images of untreated TEMPO-CNF film surface as well as the HMDSO, APTES, and hybrid APTES+HMDSO plasma-deposited surfaces are presented in Figure 5. Despite

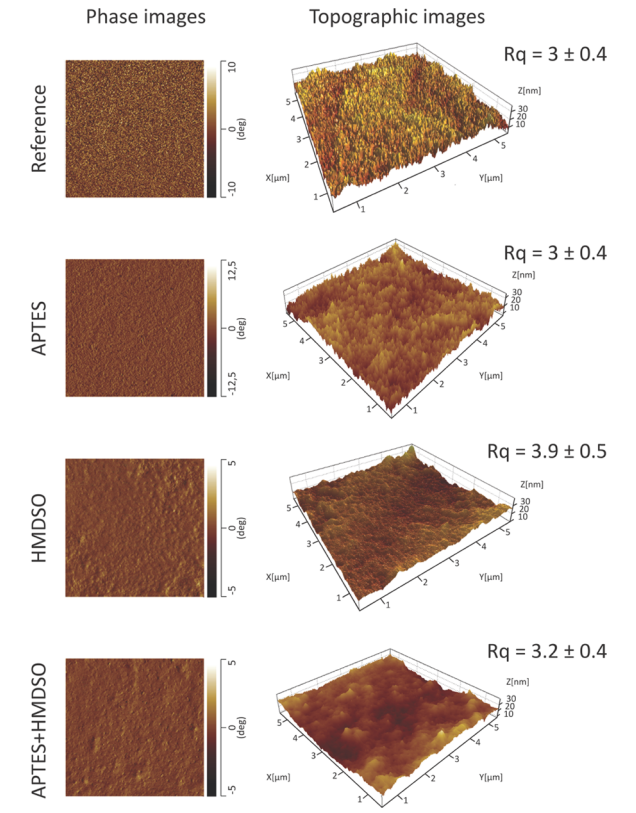

Figure 5. AFM phase contrast (left) and 3D topography images (right) for reference, HMDSO, APTES, and hybrid APTES + HMDSO plasma depositions on TEMPO-CNF films. Root-mean-square roughness (Rq) values are analyzed from 5 × 5 μm^2 images.

the thick deposited HMDSO layer, the AFM measurements revealed a smooth surface with a minor increase in roughness compared to that of bare uncoated substrate. The smooth surface and the lack of microstructures in the HMDSO deposition could indicate a layer-by-layer growth mechanism.[45] In contrast, the phase image of the deposited APTES suggests formation of layers that display somewhat globular conformation. In addition, higher roughness values were observed for the APTES-modified TEMPO-CNF substrates (~3.9 nm) compared to that found for untreated samples (~3 nm). These observations can be ascribed to the generation of particles in the depositions due to excess gas-phase reactions,[46] which have a significant role in the growth and roughness of the layers as they form clusters and act as nucleation centers around which the deposition grows.[47] This hypothesis is supported by the very smooth surface of the TEMPO-CNF substrate (~3 nm), which implies that the roughness of the APTES deposition is caused by the initial particulates, which act as preferred nucleation sites, and not by the roughness of the substrate. Finally, the topography of the hybrid APTES + HMDSO coating resembles combined features of individual APTES and HMDSO layers.

Chemical Composition of the Plasma-Deposited TEMPO-CNF Films. The chemical composition at the outmost surface of the plasma-deposited TEMPO-CNF films was assessed by X-ray photoelectron spectroscopy (XPS). To achieve higher reaction efficiency, the film surfaces were plasma-activated (without precursor monomers) prior to the deposition. This activation step efficiently removes the thin contamination/passivation layer of carbon-based compounds by instant cleavage of organic bonds.[48] Figure 6 presents the survey spectra of the modified TEMPO-CNF films, indicating that the presence of Si and N on the plasma-treated samples (silicon (Si 2p) signal is considered as a marker for successful HMDSO deposition, and silicon (Si 2p) and nitrogen (N 1s) signals for successful APTES deposition). The elemental compositions of the corresponding depositions onto TEMPO-CNF films defined by XPS analysis are summarized in Table 1. It can first be observed that all deposited layers have a substantial amount of Si, and to obtain further insight into the chemical bonds present in the plasma depositions, the high-resolution spectra recorded from the C 1s, O 1s, N 1s, and Si 2p regions are presented in Figure 6. For the HMDSO layer, the lowest-binding-energy component at ~285 eV (found in reference substrates and ascribed to saturated hydrocarbon peak due to surface contamination) in the high-resolution C 1s spectrum is significantly increased and shifted toward a lower binding energy of 284.6 eV. This shift is due to carbon atoms with silicon neighbors (such as $Si-CH_3$ and/or $Si-CH_2-CH_2$), although the components C−C and C−Si cannot be reliably resolved from each other.[49] In turn, the O 1s binding energy at ~532.5 eV suggests the formation of bonds where oxygen atoms are present also within the siloxane environment, Si−O−Si.[50] Furthermore, deconvolution of Si 2p signal confirms the presence of $CH_3-Si(-O)_3$ structures at 102.8 eV.[49,51] Considering chemical environment and relative abundance of C bonds, it is reasonable to conclude that deposited HMDSO layers consist of Si−O−Si chains that might be partly cross-linked by CH_2 groups with terminal methyl groups (CH_3) pointing upward (which are considered to be the underlying reasons for the surface hydrophobicity; see previous section).

On the other hand, the band around 285 eV in the high-resolution C 1s spectrum of APTES layer (Figure 6) increased even more significantly (compared to reference and HMDSO layer) but shifted toward a higher binding energy of 285.5 eV, which originates from carbon bonded to nitrogen (C−N).[51] In the high-resolution N 1s spectrum, two contributions can be distinguished: the main one, broad and centered at ~400.6 eV, can be attributed to nitrogen in oxime (N=C−O) and/or amide (N−C=O), whereas the other one, very minor, shifted

https://dx.doi.org/10.1021/acsabm.0c00576
ACS Appl. Bio Mater. 2020, 3, 7428−7438

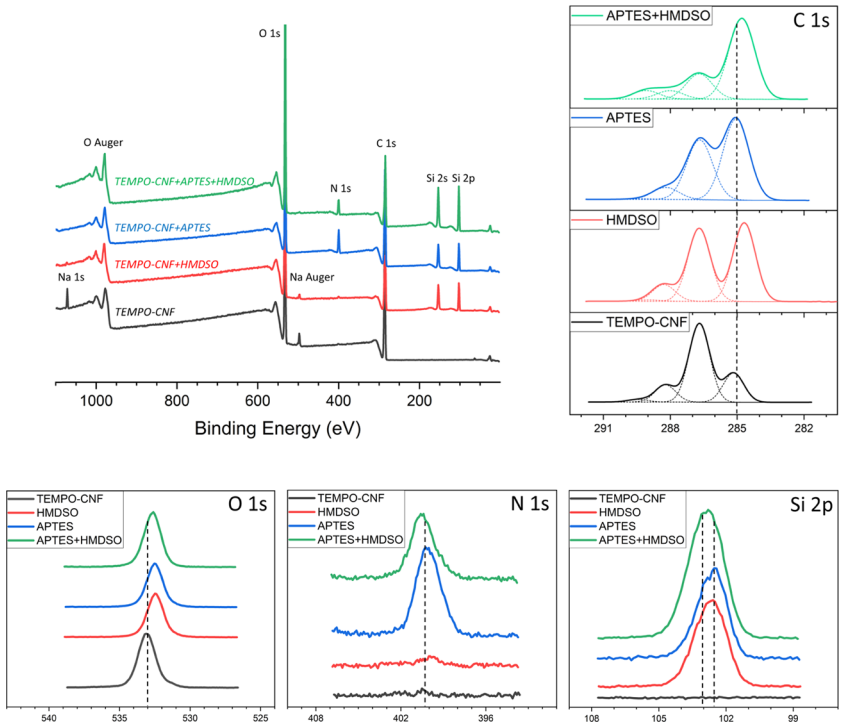

Figure 6. Low-resolution XPS survey spectra showing signals due to emission of O 1s, C 1s, N 1s, Si 2s, and Si 2p electrons (top left); high-resolution XPS spectra of the C 1s (top right), O 1s, N 1s, and Si 2p regions (bottom) for untreated (black curve), HMDSO (red curve), APTES (blue curve), and hybrid APTES + HMDSO (green curve) plasma-deposited TEMPO-CNF films. (For interpretation of the references to color in this figure legend, the reader is referred to the web version of this article).

Table 1. Elemental Surface Concentrations and Relative Abundance of Carbon Bonds for the Plasma-Modified TEMPO-CNF Films Analyzed Using XPS[a]

	elemental concentrations [atom %]						relative abundance of carbon bonds [atom %]			
sample	C 1s	O 1s	N 1s	Si 2p	O/Si	C/Si	C−C/C−Si	C−O	O−C−O	O−C═O
ref TEMPO-CNF	54.5	41.1	0.5	2.6			11.9	67.8	17.1	3.2
HMDSO	44.9	36.2	0.4	18.4	2.0	2.4	45.4	43.3	10.0	1.2
APTES	53.2	27.3	5.5	14.0	2.0	3.8	52.4	37.9	9.2	0.5
APTES + HMDSO	35.8	35.7	3.5	24.9	1.4	1.4	65.9	21.0	6.7	6.4

[a]Values are given in atomic percentage as an average of at least two measurements.

toward lower energies (399.3 eV), corresponds to C−N bonds present in amines. It is worth mentioning that obtaining aminosilane layer with terminal amine (NH_2) groups pointing away from the solid sample, thus pointing toward the liquid or gas phase, paves the way to subsequent surface modifications and/or further functionalization.[52] The Si 2p peak has broadened, and in addition to the C−Si(−O)$_3$ bonds at 102.8 eV (like in the case of pp-HMDSO), traces of other structures are found. The presence of a second contribution, which has shifted toward lower energies and centered at ∼102.2 eV, corresponds to silicon linked to two atoms of oxygen (C−Si(−O)$_2$).[53] HMDSO deposition on APTES predeposited TEMPO-CNF films resulted in a dominant contribution of C−C and C−Si bonds over other carbon bonds, accounting for 66%, Table 1. Then, carbon atomic percentages strongly decreased while the amount of silicon further increased; thus, the arrangement of deposition tends to a SiO_2-like structure. Indeed, the O/Si ratio calculated for the hybrid APTES-HMDSO coating is around 3:2, indicating that the condensation reaction is quasi-total and the highest cross-linking is obtained. In addition, a minimum value of C/Si ratio compared to HMDSO and APTES is obtained for hybrid APTES-HMDSO deposition, indicating the least branched layer is obtained. Altogether, the provided XPS observations illustrate that the initial structures of HMDSO and APTES seem to partly disappear during plasma deposition, leading to evolution of Si(−O)$_4$ and C−Si(−O)$_3$ structures. These structures are related to the inorganic character of the depositions, which are also associated with their hardness,[53] wear resistance,[54] as well as gas barrier properties.[21]

CONCLUSIONS

We demonstrate a combination of NIL and atmospheric plasma deposition technique as a fast, robust, and industrially scalable (both are R2R processes) approach for tailoring the surface properties of TEMPO-CNF films. NIL patterning was effective in creating uniform pillars on the cellulosic films. Further deposition of plasma-polymerized layers resulted in surface hydrophobicity. For instance, the water contact angle increased from ∼20° for untreated TEMPO-CNF films to ∼105° for the HMDSO plasma-deposited sample and further up to ∼120° for the HMDSO plasma treated after NIL patterning; likewise, the surface energy changed from 46−50 to

https://dx.doi.org/10.1021/acsabm.0c00576
ACS Appl. Bio Mater. 2020, 3, 7428−7438

~29 mJ/m^2 and became ~22 mJ/m^2 (represented entirely by the dispersive component) for the HMDSO plasma-coated after NIL patterning. Deposition of APTES, on the other hand, did not produce major benefits for surface wettability, possibly due to the introduction of amine functionalities. XPS, AFM, and SEM investigations indicated deposition of predominantly inorganic (Si(−O)4 and C−Si(−O)3 structures), uniform and smooth depositions onto TEMPO-CNF films. As a result, continuous layers that effectively hamper the water−cellulose interactions and simultaneously have low affinity toward oxygen were formed while maintaining the bulk properties of the substrates. Moreover, that allowed preserving an excellent light transmittance (88−89% at 550 nm) of TEMPO-CNF films with the possibility of tuning optical haze due to NIL surface patterning. Overall, it is evidenced that surface modification of TEMPO-CNF films employing NIL and plasma deposition processes allows tailoring hydrophobic/hydrophilic balance, optical properties, gas and moisture permeabilities simultaneously. These findings pave the way toward advanced material solutions from sustainable nanocellulose-based sources comprising smart multifunctional films for, e.g., packaging, optics, immunodiagnostics, and electronics.

EXPERIMENTAL SECTION

TEMPO-CNF Film Preparation by Cast-Coating Using an R2R Manufacturing Unit. Commercial bleached softwood kraft pulp (spruce/pine mix) obtained from a Finnish pulp mill was used as a raw material for the preparation of cellulose nanofibrils. TEMPO-mediated oxidation of the pulp fibers was carried out by alkaline oxidation with hypochlorite catalyzed by TEMPO, according to the protocol described by Saito et al.[55] The degree of oxidation per anhydroglucose unit of cellulose was at the level of 1.2 mmol/g. The TEMPO-oxidized pulp suspension was purified and further fibrillated into TEMPO-CNF using a microfluidizer (Microfluidics International) equipped with two Z-type chambers with respective diameters of 400 and 100 mm. The fibrillation was done in two passes at 1850 bar operating pressure, and the final consistency of the TEMPO-CNF film was ~1 wt %.

The TEMPO-CNF film production is based on cast-coating of the gel-type TEMPO-CNF suspension with precise control of adhesion, spreading, and drying of TEMPO-CNF on a supporting plastic substrate.[56] Briefly, a defined amount of TEMPO-CNF suspension with strength additive and softener is applied on a pretreated plastic substrate in a semi-pilot-scale commercial converting unit. After evaporation of the excess of solvent by controlled drying, the TEMPO-CNF film was then carefully separated from the plastic substrate as a self-standing structure. Sorbitol (30 wt % solids in dry film from Sigma-Aldrich) was used as a softener to improve the flexibility of TEMPO-CNF films. In addition, due to the very brittle character of the TEMPO-CNF films, polyvinyl alcohol (PVA, Moviol 56-98, M_w 195 000, 10 wt % solids in dry film from Sigma-Aldrich) was used to enhance the strength properties of the TEMPO-CNF films. The final thickness values of the TEMPO-CNF films varied between 20 and 25 μm.

Roll-to-Roll Nanoimprint Lithography (NIL) of TEMPO-CNF Films. Micropillars were constructed on TEMPO-CNF films using roll-to-roll nanoimprinting (R2RNIL) experiments, as described in detail by Mäkelä et al.[44] In the imprinting roll, the flexible Ni-mold was wrapped on a metallic roll and heated by an electrical heater located inside the roll. A flexible Ni-mold was clamped mechanically on the upper metal roll and heated to the printing temperature, while the backing roll was kept at room temperature. The printing force between the rolls was 900 N, which corresponded to a pressure of 8.3 MPa and the printing speed was 0.2 ± 0.1 m/min. In these experiments, the surface temperature of the mold was fixed to 130 ± 1 °C and was measured each time before the NIL experiment using a k-type thermoelement sensor. The mold was cleaned with isopropanol (semiconductor grade from Sigma-Aldrich) before each experiment and during the experiments if any contamination was visible. Prior to NIL experiments, samples were stored for at least 1 day at room atmosphere (23 °C and a relative humidity varying between 35 and 45%).

Interfacial Modification of TEMPO-CNF Films by Plasma-Assisted Gas-Phase Reaction. Surface modification of already assembled TEMPO-CNF films was carried out by means of a Plasmaline atmospheric plasma-enhanced chemical vapor deposition unit. For that, (3-aminopropyl)triethoxysilane (APTES, 97% from Sigma-Aldrich) and hexamethyldisiloxane (HMDSO, >99% from Sigma-Aldrich) were used as precursor molecules. Briefly, to proceed with the thin-film deposition, a mixture consisting of the carrier gas nitrogen (N_2 feed flow = 2 × 150 slm) and the monomer gas (precursor feed = 2 × 1.2 slm) was passed between the two electrodes in a plasma reactor. The monomer vapor was produced via a glass bubbler containing precursor chemicals, in which nitrogen was introduced as a secondary flow (N_2 additive flow = 2 × 2 slm). The plasma power, line speed, and number of passes were set to 400 W, 0.5 m/min, and 4, respectively. Prior to the surface chemical modification step, the CNF film surface was activated using the same process parameters but without chemical feed. This activation step efficiently removes the thin contamination/passivation layer of carbon-based compounds by instant cleavage of organic bonds and thus leads to higher reaction efficiency.[48]

Characterization. *Physical Properties.* The transmittance spectrum and haze of TEMPO-CNF films were measured with a Cary 5000 UV−vis−NIR spectrophotometer (Agilent Technologies) between 800 and 200 nm at a scan rate of 600 nm/min and data interval of 1 nm; haze measurement was carried out according to ASTM D1003 "Standard Method for Haze and Luminous Transmittance of Transparent Plastics" using an integrating sphere (DRA 2500, Agilent), which is defined as[57] (eq 1)

$$\text{haze} = \left(\frac{T4}{T2} - \frac{T3}{T1}\right) \times 100\% \tag{1}$$

where $T1$, $T2$, $T3$, and $T4$ are changing configurations of the sample placement on the sphere, as shown elsewhere.[29]

The surface energy, SE, its components, and the interfacial free energy of plasma-deposited TEMPO-CNF films were assessed using contact angle (CA) measurements with four probing liquids with known surface energy (ethylene glycol, water, diiodomethane, and formamide). Calculations were done using Young's equation (CA data) and the solid/liquid interfacial energy according to eq 2

$$\frac{(1+\cos\theta)\gamma_l}{2} = \sqrt{\gamma_s^d \gamma_l^d} + \sqrt{\gamma_s^- \gamma_l^+} + \sqrt{\gamma_s^+ \gamma_l^-} \tag{2}$$

This method derives dispersive (γ_s^d) and polar (acid−base) contributions of a solid material. The latter is further divided into γ_s^+, the electron acceptor or Lewis acid parameter, and γ_s^-, the electron donor or Lewis base parameter.

Moreover, the interfacial free energy of the films (ΔG_{sws}^{IFE}) was evaluated to verify the nature (hydrophobic or hydrophilic) of the surface.[58] ΔG_{sws}^{IFE} is the energy of interaction between particles or molecules of a solid material (s) immersed in a liquid (water, w) and is defined as

$$\Delta G_{sws}^{IFE} = -2\gamma_{sw} = -2\cdot(\gamma_{sw}^D + \gamma_{sw}^P) \tag{3}$$

The dispersive (Lifshitz−van der Waals interactions) component of interfacial tension is related to the individual surface tension of the solid material (s) and water (w) according to the Good−Girifalco−Fowkes rule[59]

$$\gamma_{sw}^D = (\sqrt{\gamma_s^D} - \sqrt{\gamma_w^D})^2 \tag{4}$$

The polar component of the interfacial tension between s and w can be expressed as

$$\gamma_{sw}^p = 2\cdot(\sqrt{\gamma_s^+\gamma_s^-} + \sqrt{\gamma_w^+\gamma_w^-} - \sqrt{\gamma_s^+\gamma_w^-} - \sqrt{\gamma_w^+\gamma_s^-}) \tag{5}$$

https://dx.doi.org/10.1021/acsabm.0c00576
ACS Appl. Bio Mater. 2020, 3, 7428−7438

The CA of sessile drops on the depositions was determined using a CAM200 optical contact angle goniometer (KSV Instruments Ltd, Finland). The tests were performed at 23 °C and 50% relative humidity (RH), and the results are presented as an average value of three to five experiments.

Oxygen transmission rate (OTR) through the modified films was determined with an Oxygen Permeation Analyzer Model 8101 (Systech Instruments Ltd, U.K.) according to standard ASTM D3985. All samples were equilibrated overnight, and the tests were carried out the next day using 100% oxygen as a probing gas at 23 °C and 80% RH applying metal masks with a test area of 5 cm^2. Four duplicate measurements were carried out. Oxygen permeability (OP) was then calculated as (by multiplying the OTR value with the sample thickness of the sample and then dividing by sea-level pressure)

$$\mathrm{OP} = \frac{\mathrm{OTR}\cdot\mathrm{thickness}}{\text{oxygen partial pressure difference}} \quad (6)$$

Water vapor transmission rates (WVTR) were determined gravimetrically using a modified ASTM-E-96 B procedure "dry cup method". Samples with a test area of 30 cm^2 were mounted on circular aluminum cups (68−3000 Vapometer EZ-Cups; Thwing-Albert Instrument Company) containing anhydrous $CaCl_2$ (0% relative humidity). The cups were stored in test conditions of 23 °C and 50% RH and weighed periodically until a constant rate of weight reduction was attained. In this test, 50/0% relative humidity gradient (the driving force for water molecules to diffuse within a material) was used. Four duplicate measurements were carried out. Water vapor permeability (WVP) was then obtained as (by multiplying WVTR with the sample thickness and then dividing by the water vapor difference across the film)

$$\mathrm{WVP} = \frac{\mathrm{WVTR}\cdot\mathrm{thickness}}{\text{saturated pressure}\cdot\%\mathrm{RH}} \quad (7)$$

Surface Morphology. The surface and cross section of modified TEMPO-CNF films were investigated with a Zeiss Merlin FE-SEM (Carl Zeiss NTS GmbH, Germany). The imaging was performed with a 1.5 keV electron energy using both InLens and secondary electron detectors. The cross sections were prepared using a Leica RM2255 rotation microtome. Prior to SEM characterization, all samples were platinum sputter-coated (Leica EM ACE200) at 30 mA for 30 s (thickness ∼ 2 nm). The image pixel resolution was 2048 × 1536. Surface morphology and roughness of the films were analyzed by ANASYS AFM+ atomic force microscope (ANASYS Instruments, Inc., Santa Barbara, CA, USA). The images were taken in tapping mode in air using aluminum-coated n-type silicon cantilevers (HQ:NSC15/Al BS, Micromasch, Tallinn, Estonia) with a typical probe radius of 8 nm, a force constant of 40 N/m, and nominal resonance frequencies between 265 and 410 kHz. The surface of each sample was imaged in at least three different places, and the images were not processed in any way. The surface roughness parameter (Rq) was determined from the raw data using Park Systems XEI 1.7.5 image analysis software.

Surface Chemical Analysis. Surface chemical analysis of the modified films was investigated using X-ray photoelectron spectroscopy (XPS) with a Kratos Analytical AXIS Ultra electron spectrometer with monochromatic A1 Kα irradiation at 100 W utilizing the experimental procedure tailored for cellulosic materials.[60] Elemental surface composition was determined from low-resolution survey scans, while high-resolution measurements of carbon (C 1s), oxygen (O 1s), silicon (Si 2p), and nitrogen (N 1s) regions were applied for a more detailed chemical evaluation. Two to three locations were measured for each sample with a nominal analysis area of 300 × 700 μm^2 and an analysis depth of less than 10 nm. Ash-free pure cellulose filter paper (Whatman) was used as *in situ* reference with each measurement batch. CasaXPS software was utilized for data analysis, the main cellulosic carbon component, C−O at 286.7 eV, was used in binding-energy corrections for all of the spectra, and for the carbon regions, a specific four-component fitting routine tailored for cellulosic specimen was applied.[61] No sample degradation due to ultrahigh vacuum or X-rays was observed.

■ ASSOCIATED CONTENT

Supporting Information

The Supporting Information is available free of charge at https://pubs.acs.org/doi/10.1021/acsabm.0c00576.

Surface energies and water contact angles of NIL surface-patterned and APTES and hybrid APTES + HMDSO plasma-deposited TEMPO-CNF films; surface free-energy parameters for the liquid probes and calculated surface energy components; and affinity to water ΔG_{sws}^{IFE} for plasma-deposited TEMPO-CNF films with and without NIL surface patterning (PDF)

■ AUTHOR INFORMATION

Corresponding Authors

Alexey Khakalo − *VTT Technical Research Centre of Finland Ltd., FI-02044 Espoo, Finland;* orcid.org/0000-0001-7631-9606; Phone: +358504018149; Email: alexey.khakalo@vtt.fi

Tekla Tammelin − *VTT Technical Research Centre of Finland Ltd., FI-02044 Espoo, Finland;* orcid.org/0000-0002-3248-1801; Phone: +358207224632; Email: tekla.tammelin@vtt.fi

Authors

Tapio Mäkelä − *VTT Technical Research Centre of Finland Ltd., FI-02150 Espoo, Finland*

Leena-Sisko Johansson − *Department of Bioproducts and Biosystems, School of Chemical Engineering, Aalto University, FI-00076 Aalto, Finland*

Hannes Orelma − *VTT Technical Research Centre of Finland Ltd., FI-02044 Espoo, Finland;* orcid.org/0000-0001-5070-9542

Complete contact information is available at: https://pubs.acs.org/10.1021/acsabm.0c00576

Author Contributions

This manuscript was written through contributions of all authors. All authors have given approval to the final version of the manuscript.

Notes

The authors declare no competing financial interest.

■ ACKNOWLEDGMENTS

This project has received funding from the European Union's Horizon 2020 research and innovation programme under grant agreement no. 760876. Mykola Ivanchenko and Unto Tapper are thanked for carrying out the cross section preparations for SEM imaging; Juha Mannila is acknowledged for assisting with plasma deposition process; Vuokko Liukkonen, Katja Pettersson, and Hille Rautkoski are thanked for performing contact angle, AFM, and barrier measurements, respectively. This work was part of the Academy of Finland Flagship Programme under project nos. 318890 and 318891 (Competence Center for Materials Bioeconomy, FinnCERES).

■ REFERENCES

(1) Zhu, H.; Luo, W.; Ciesielski, P. N.; Fang, Z.; Zhu, J. Y.; Henriksson, G.; Himmel, M. E.; Hu, L. Wood-Derived Materials for Green Electronics, Biological Devices, and Energy Applications. *Chem. Rev.* **2016**, 9305−9374.

(2) Kontturi, E.; Laaksonen, P.; Linder, M. B.; Nonappa; Gröschel, A. H.; Rojas, O. J.; Ikkala, O. Advanced Materials through Assembly of Nanocelluloses. *Adv. Mater.* **2018**, *30*, No. 1703779.
(3) Eichhorn, S. J.; Dufresne, A.; Aranguren, M.; Marcovich, N. E.; Capadona, J. R.; Rowan, S. J.; Weder, C.; Thielemans, W.; Roman, M.; Renneckar, S.; Gindl, W.; Veigel, S.; Keckes, J.; Yano, H.; Abe, K.; Nogi, M.; Nakagaito, A. N.; Mangalam, A.; Simonsen, J.; Benight, A. S.; Bismarck, A.; Berglund, L. A.; Peijs, T. *Review: Current International Research into Cellulose Nanofibres and Nanocomposites*; Springer: US, 2010; Vol. *45*, pp 1−33.
(4) Klemm, D.; Kramer, F.; Moritz, S.; Lindström, T.; Ankerfors, M.; Gray, D.; Dorris, A. Nanocelluloses: A New Family of Nature-Based Materials. *Angew. Chem., Int. Ed.* **2011**, *50*, 5438−5466.
(5) Moon, R. J.; Martini, A.; Nairn, J.; Simonsen, J.; Youngblood, J. Cellulose Nanomaterials Review: Structure, Properties and Nanocomposites. *Chem. Soc. Rev.* **2011**, *40*, 3941−3994.
(6) Jin, H.; Marin, G.; Giri, A.; Tynell, T.; Gestranius, M.; Wilson, B. P.; Kontturi, E.; Tammelin, T.; Hopkins, P. E.; Karppinen, M. Strongly Reduced Thermal Conductivity in Hybrid ZnO/Nanocellulose Thin Films. *J. Mater. Sci.* **2017**, *52*, 6093−6099.
(7) Jämsä, M.; Kosourov, S.; Rissanen, V.; Hakalahti, M.; Pere, J.; Ketoja, J. A.; Tammelin, T.; Allahverdiyeva, Y. Versatile Templates from Cellulose Nanofibrils for Photosynthetic Microbial Biofuel Production. *J. Mater. Chem. A* **2018**, *6*, 5825−5835.
(8) Orelma, H.; Hokkanen, A.; Leppänen, I.; Kammiovirta, K.; Kapulainen, M.; Harlin, A. Optical Cellulose Fiber Made from Regenerated Cellulose and Cellulose Acetate for Water Sensor Applications. *Cellulose* **2020**, *27*, 1543−1553.
(9) Isogai, A.; Saito, T.; Fukuzumi, H. TEMPO-Oxidized Cellulose Nanofibers. *Nanoscale.* **2011**, *3*, 71−85.
(10) Fang, Z.; Zhu, H.; Yuan, Y.; Ha, D.; Zhu, S.; Preston, C.; Chen, Q.; Li, Y.; Han, X.; Lee, S.; Chen, G.; Li, T.; Munday, J.; Huang, J.; Hu, L. Novel Nanostructured Paper with Ultrahigh Transparency and Ultrahigh Haze for Solar Cells. *Nano Lett.* **2014**, *14*, 765−773.
(11) Zhu, H.; Fang, Z.; Wang, Z.; Dai, J.; Yao, Y.; Shen, F.; Preston, C.; Wu, W.; Peng, P.; Jang, N.; Yu, Q.; Yu, Z.; Hu, L. Extreme Light Management in Mesoporous Wood Cellulose Paper for Optoelectronics. *ACS Nano* **2016**, *10*, 1369−1377.
(12) Ou, Y.; Chen, J.; Lu, P.; Cheng, F.; Lin, M.; Su, L.; Li, J.; Liu, D. Rapid ILs-Polishing Processes Toward Flexible Nanostructured Paper with Dually High Transparency and Haze. *Sci. Rep.* **2017**, *7*, No. 6942.
(13) Yang, W.; Jiao, L.; Liu, W.; Deng, Y.; Dai, H. Morphology Control for Tunable Optical Properties of Cellulose Nanofibrils Films. *Cellulose* **2018**, *25*, 5909−5918.
(14) Mäkelä, T.; Hokkanen, A.; Sneck, A.; Ruotsalainen, T.; Khakalo, A.; Tammelin, T. Vapour-Assisted Roll-to-Roll Nanoimprinting of Micropillars on Nanocellulose Films. *Microelectron. Eng.* **2020**, *225*, No. 111258.
(15) Martinez, A. W.; Phillips, S. T.; Whitesides, G. M.; Carrilho, E. Diagnostics for the Developing World: Microfluidic Paper-Based Analytical Devices. *Anal. Chem.* **2010**, *82*, 3−10.
(16) Forsman, N.; Lozhechnikova, A.; Khakalo, A.; Johansson, L.-S. L. S.; Vartiainen, J.; Österberg, M. Layer-by-Layer Assembled Hydrophobic Coatings for Cellulose Nanofibril Films and Textiles, Made of Polylysine and Natural Wax Particles. *Carbohydr. Polym.* **2017**, *173*, 392−402.
(17) Milionis, A.; Sharma, C. S.; Hopf, R.; Uggowitzer, M.; Bayer, I. S.; Poulikakos, D. Engineering Fully Organic and Biodegradable Superhydrophobic Materials. *Adv. Mater. Interfaces* **2019**, *6*, No. 1801202.
(18) Bárdos, L.; Baránková, H. Cold Atmospheric Plasma: Sources, Processes, and Applications. *Thin Solid Films.* **2010**, *518*, 6705−6713.
(19) Corbella, C. Upscaling Plasma Deposition: The Influence of Technological Parameters. *Surf. Coat. Technol.* **2014**, *242*, 237−245.
(20) Siliprandi, R. A.; Zanini, S.; Grimoldi, E.; Fumagalli, F. S.; Barni, R.; Riccardi, C. Atmospheric Pressure Plasma Discharge for Polysiloxane Thin Films Deposition and Comparison with Low Pressure Process. *Plasma Chem. Plasma Process.* **2011**, *31*, 353−372.
(21) Grimoldi, E.; Zanini, S.; Siliprandi, R. A.; Riccardi, C. AFM and Contact Angle Investigation of Growth and Structure of Pp-HMDSO Thin Films. *Eur. Phys. J., D* **2009**, *54*, 165−172.
(22) Ziari, Z.; Nouicer, I.; Sahli, S.; Rebiai, S.; Bellel, A.; Segui, Y.; Raynaud, P. Chemical and Electrical Properties of HMDSO Plasma Coated Polyimide. *Vacuum* **2013**, *93*, 31−36.
(23) Cho, S. G. C.; Hong, Y. C.; Cho, S. G. C.; Ji, Y. Y.; Han, C. S.; Uhm, H. S. Surface Modification of Polyimide Films, Filter Papers, and Cotton Clothes by HMDSO/Toluene Plasma at Low Pressure and Its Wettability. *Curr. Appl. Phys.* **2009**, *9*, 1223−1226.
(24) Gueye, M.; Gries, T.; Noël, C.; Migot-Choux, S.; Bulou, S.; Lecoq, E.; Choquet, P.; Kutasi, K.; Belmonte, T. Interaction of (3-Aminopropyl)Triethoxysilane with Pulsed Ar−O2 Afterglow: Application to Nanoparticles Synthesis. *Plasma Chem. Plasma Process.* **2016**, *36*, 1031−1050.
(25) Zhang, D. X.; Yoshikawa, C.; Welch, N. G.; Pasic, P.; Thissen, H.; Voelcker, N. H. Spatially Controlled Surface Modification of Porous Silicon for Sustained Drug Delivery Applications. *Sci. Rep.* **2019**, *9*, No. 1367.
(26) Peresin, M. S.; Kammiovirta, K.; Heikkinen, H.; Johansson, L. S.; Vartiainen, J.; Setälä, H.; Österberg, M.; Tammelin, T. Understanding the Mechanisms of Oxygen Diffusion through Surface Functionalized Nanocellulose Films. *Carbohydr. Polym.* **2017**, *174*, 309−317.
(27) Fukuzumi, H.; Saito, T.; Iwata, T.; Kumamoto, Y.; Isogai, A. Transparent and High Gas Barrier Films of Cellulose Nanofibers Prepared by TEMPO-Mediated Oxidation. *Biomacromolecules* **2009**, *10*, 162−165.
(28) Toomre, D.; Manstein, D. J. Lighting up the Cell Surface with Evanescent Wave Microscopy. *Trends Cell Biol.* **2001**, *11*, 298−303.
(29) Li, Y.; Fu, Q.; Yu, S.; Yan, M.; Berglund, L. Optically Transparent Wood from a Nanoporous Cellulosic Template: Combining Functional and Structural Performance. *Biomacromolecules* **2016**, *17*, 1358−1364.
(30) Lassen, B.; Malmsten, M. Competitive Protein Adsorption at Plasma Polymer Surfaces. *J. Colloid Interface Sci.* **1997**, *186*, 9−16.
(31) Lee, M. H.; Brass, D. A.; Morris, R.; Composto, R. J.; Ducheyne, P. The Effect of Non-Specific Interactions on Cellular Adhesion Using Model Surfaces. *Biomaterials* **2005**, *26*, 1721−1730.
(32) Yang, W.; Jiao, L.; Liu, W.; Dai, H. Manufacture of Highly Transparent and Hazy Cellulose Nanofibril Films via Coating TEMPO-Oxidized Wood Fibers. *Nanomaterials* **2019**, *9*, 107.
(33) Van Lare, C.; Lenzmann, F.; Verschuuren, M. A.; Polman, A. Dielectric Scattering Patterns for Efficient Light Trapping in Thin-Film Solar Cells. *Nano Lett.* **2015**, *15*, 4846−4852.
(34) Gardner, D. J.; Han, Y.; Tshabalala, M. A.; Peng, Y.; Cai, Z. Influence of Drying Method on the Surface Energy of Cellulose Nanofibrils Determined by Inverse Gas Chromatography. *J. Colloid Interface Sci.* **2013**, *405*, 85−95.
(35) Miwa, M.; Nakajima, A.; Fujishima, A.; Hashimoto, K.; Watanabe, T. Effects of the Surface Roughness on Sliding Angles of Water Droplets on Superhydrophobic Surfaces. *Langmuir* **2000**, *16*, 5754−5760.
(36) Feng, X.; Jiang, L. Design and Creation of Superwetting/Antiwetting Surfaces. *Adv. Mater.* **2006**, *18*, 3063−3078.
(37) Österberg, M.; Peresin, M. S.; Johansson, L. S.; Tammelin, T. Clean and Reactive Nanostructured Cellulose Surface. *Cellulose* **2013**, *20*, 983−990.
(38) Chinga-Carrasco, G.; Kuznetsova, N.; Garaeva, M.; Leirset, I.; Galiullina, G.; Kostochko, A.; Syverud, K. Bleached and Unbleached MFC Nanobarriers: Properties and Hydrophobisation with Hexamethyldisilazane. *J. Nanopart. Res.* **2012**, *14*, No. 1280.
(39) Kayaoğlu, B. K.; Öztürk, E. Imparting Hydrophobicity to Natural Leather through Plasma Polymerization for Easy Care Effect. *Fibers Polym.* **2013**, *14*, 1706−1713.
(40) Sunkara, V.; Park, D. K.; Cho, Y. K. Versatile Method for Bonding Hard and Soft Materials. *RSC Adv.* **2012**, *2*, 9066−9070.
(41) Schweiger, S.; Neubauer, C.; Fraser, S. D.; Klein, T.; Schennach, R.; Reichmann, A.; Gruber-Woelfler, H. Coating of

https://dx.doi.org/10.1021/acsabm.0c00576
ACS Appl. Bio Mater. 2020, 3, 7428−7438

Glass Substrates to Prevent Alkali Ion Diffusion into Pharmaceutical Solutions. *Surf. Coat. Technol.* **2014**, *258*, 1249−1255.
(42) Lavoine, N.; Desloges, I.; Dufresne, A.; Bras, J. Microfibrillated Cellulose - Its Barrier Properties and Applications in Cellulosic Materials: A Review. *Carbohydr. Polym.* **2012**, *90*, 735−764.
(43) Takeda, S.; Fukawa, M.; Hayashi, Y.; Matsumoto, K. Surface OH Group Governing Adsorption Properties of Metal Oxide Films. *Thin Solid Films* **1999**, *339*, 220−224.
(44) Mäkelä, T.; Kainlauri, M.; Willberg-Keyriläinen, P.; Tammelin, T.; Forsström, U. Fabrication of Micropillars on Nanocellulose Films Using a Roll-to-Roll Nanoimprinting Method. *Microelectron. Eng.* **2016**, *163*, 1−6.
(45) Teshima, K.; Inoue, Y.; Sugimura, H.; Takai, O. Growth and Structure of Silica Films Deposited on a Polymeric Material by Plasma-Enhanced Chemical Vapor Deposition. *Thin Solid Films* **2002**, *Vol. 420−421*, 324−329.
(46) Ramamoorthy, A.; Rahman, M.; Mooney, D. A.; Don MacElroy, J. M.; Dowling, D. P. The Influence of Process Parameters on Chemistry, Roughness and Morphology of Siloxane Films Deposited by an Atmospheric Plasma Jet System. *Plasma Processes Polym.* **2009**, *6*, S530−S536.
(47) Wuu, D. S.; Lo, W. C.; Chiang, C. C.; Lin, H. B.; Chang, L. S.; Horng, R. H.; Huang, C. L.; Gao, Y. J. Plasma-Deposited Silicon Oxide Barrier Films on Polyethersulfone Substrates: Temperature and Thickness Effects. *Surf. Coat. Technol.* **2005**, *197*, 253−259.
(48) Johansson, L. S.; Tammelin, T.; Campbell, J. M.; Setälä, H.; Österberg, M. Experimental Evidence on Medium Driven Cellulose Surface Adaptation Demonstrated Using Nanofibrillated Cellulose. *Soft Matter* **2011**, *7*, 10917−10924.
(49) Alexander, M. R.; Short, R. D.; Jones, F. R.; Michaeli, W.; Blomfield, C. J. A Study of HMDSO/O 2 Plasma Deposits Using a High-Sensitivity and -Energy Resolution XPS Instrument: Curve Fitting of the Si 2p Core Level. *Appl. Surf. Sci.* **1999**, *137*, 179−183.
(50) Alexander, M. R.; Short, R. D.; Jones, F. R.; Stollenwerk, M.; Zabold, J.; Michaeli, W. An X-Ray Photoelectron Spectroscopic Investigation into the Chemical Structure of Deposits Formed from Hexamethyldisiloxane/Oxygen Plasmas. *J. Mater. Sci.* **1996**, *31*, 1879−1885.
(51) Lecoq, E.; Duday, D.; Bulou, S.; Frache, G.; Hilt, F.; Maurau, R.; Choquet, P. Plasma Polymerization of APTEs to Elaborate Nitrogen Containing Organosilicon Thin Films: Influence of Process Parameters and Discussion about the Growing Mechanisms. *Plasma Process. Polym.* **2013**, *10*, 250−261.
(52) Acres, R. G.; Ellis, A. V.; Alvino, J.; Lenahan, C. E.; Khodakov, D. A.; Metha, G. F.; Andersson, G. G. Molecular Structure of 3-Aminopropyltriethoxysilane Layers Formed on Silanol-Terminated Silicon Surfaces. *J. Phys. Chem. C* **2012**, *116*, 6289−6297.
(53) Lin, Y.-S.; Weng, M. S.; Chung, T. W.; Huang, C. Enhanced Surface Hardness of Flexible Polycarbonate Substrates Using Plasma-Polymerized Organosilicon Oxynitride Films by Air Plasma Jet under Atmospheric Pressure. *Surf. Coat. Technol.* **2011**, *205*, 3856−3864.
(54) Meškinis, Š.; Tamulevičiene, A. Structure, Properties and Applications of Diamond like Nanocomposite (SiO x Containing DLC) Films: A Review. *Medziagotyra.* **2011**, *17*, 358−370.
(55) Saito, T.; Nishiyama, Y.; Putaux, J. L.; Vignon, M.; Isogai, A. Homogeneous Suspensions of Individualized Microfibrils from TEMPO-Catalyzed Oxidation of Native Cellulose. *Biomacromolecules* **2006**, *7*, 1687−1691.
(56) Tammelin, T.; Hippi, U.; Salminen, A. Method for the Preparation of Nanofibrillated Cellulose (NFC) Films on Supports. WO. Patent WO2013/0609342013.
(57) ASTM International. *Standard Test Method for Haze and Luminous Transmittance of Transparent Plastics*; ASTM D1003, 2003; pp 1−6.
(58) Van Oss, C. J.; Chaudhury, M. K.; Good, R. J. Interfacial Lifshitz-van Der Waals and Polar Interactions in Macroscopic Systems. *Chem. Rev.* **1988**, *88*, 927−941.
(59) Good, R. J.; Girifalco, L. A. A Theory for Estimation of Surface and Interfacial Energies. III. Estimation of Surface Energies of Solids from Contact Angle Data. *J. Phys. Chem. A* **1960**, *64*, 561−565.
(60) Johansson, L. S. Monitoring Fibre Surfaces with XPS in Papermaking Processes. *Mikrochim. Acta* **2002**, *Vol. 138−139*, 217−223.
(61) Johansson, L. S.; Campbell, J. M. Reproducible XPS on Biopolymers: Cellulose Studies. *Surf. Interface Anal.* **2004**, *36*, 1018−1022.

https://dx.doi.org/10.1021/acsabm.0c00576
ACS Appl. Bio Mater. 2020, 3, 7428−7438